CHEMIJA
2025. Vol. 36. No. 3. P. 161–176

ISSN 0235-7216 eISSN 2424-4538
DOI: https://doi.org/10.6001/chemija.2025.36.3.6

Effect of graphite particle size on the physicochemical properties and dopamine-sensing performance of reduced graphene oxide

Dovilė Burakovaitė[1],

Rūta Rasikė[1],

Vilius Čižas[1],

Gediminas Niaura[2],

Tomas Murauskas[1],

Rasa Pauliukaitė[1, 3],

Justina Gaidukevič[1, 3*]

[1] *Institute of Chemistry,*
Faculty of Chemistry and Geosciences,
Vilnius University,
24 Naugarduko Street,
03225 Vilnius, Lithuania

[2] *Department of Organic Chemistry,*
Center for Physical Sciences and Technology,
3 Saulėtekio Avenue,
10257 Vilnius, Lithuania

[3] *Department of Nanoengineering,*
Center for Physical Sciences and Technology,
231 Savanorių Avenue,
02300 Vilnius, Lithuania

Graphene oxide (GO) was synthesised from graphite powders of two different particle sizes (≤50 and ≥149–≤840 μm) using the Hummers' method and subsequently reduced by thermal shock at 800°C to obtain reduced graphene oxide (rGO). The obtained samples, denoted rGO_1 (from smaller graphite particles) and rGO_2 (from larger graphite flakes), were investigated to evaluate the influence of precursor size on their physicochemical properties and electrochemical performance. Structural characterisation was carried out by X-ray photoelectron spectroscopy, Raman spectroscopy, X-ray diffraction, scanning electron microscopy and nitrogen adsorption–desorption analysis. The results confirmed the removal of oxygen-containing groups after thermal reduction and indicated differences in crystallite domains and defect density depending on the size of the graphite precursor. Electrochemical measurements demonstrated that both samples were able to detect dopamine (DA). The electrodes showed linear DA detection in a concentration range of 1–19.96 μM, with detection limits of 61.55 nM for rGO_1 and 98.17 nM for rGO_2. Sensitivities were determined as 6.44 and 12.20 μA μM^{-1} cm^{-2}, respectively. Our results suggest that the properties of rGO can be tailored by controlling the size of the graphite precursor, which may provide new opportunities for the design of rGO-based electrochemical sensors.

Keywords: reduced graphene oxide, graphite particle size, dopamine detection, electrochemical sensors

INTRODUCTION

Graphene oxide (GO) has attracted a significant attention in recent years due to its unique structural and chemical properties derived from its layered graphene framework enriched with oxygen-containing functional groups. These groups provide tunable physicochemical properties and improve the material's suitability for further functionalisation. GO is typically synthesised from graphite by oxidation, and its physicochemical properties can be tuned by parameters such as the size of the precursor graphite flakes. Additional modification can be achieved through thermal reduction to reduced graphene oxide (rGO), a process that partially restores the graphene lattice while altering the surface

* Corresponding author. Email: justina.gaidukevic@chf.vu.lt

chemistry [1–3]. These graphene-based materials have shown a great promise in various applications, such as energy storage [4], electronic and optoelectronic devices [5], catalysis [6, 7], environmental protection [8], as well as exceptional potential in analytical fields, particularly electrochemical sensing [9, 10]. Key features of these materials, such as an extremely high surface area, an excellent electrical conductivity and a rich chemical reactivity, facilitate an efficient electron transfer and provide abundant active sites for analyte interaction. These characteristics make GO, rGO and their derivatives ideal candidates for detecting biologically important molecules, environmental pollutants and chemical substances [10, 11]. Among these, the neurotransmitter dopamine (DA) has attracted the greatest research attention because of its vital role in regulating neurological processes and its relevance in diagnosing various neurodegenerative and psychiatric disorders [12]. The development of accurate, sensitive and selective electrochemical DA sensors is therefore of paramount importance for the timely detection, early intervention and effective management of diseases such as Parkinson's, Alzheimer's, depression and schizophrenia.

Numerous studies have established that the performance of graphene-based sensors in neurotransmitter detection arises from the synergy between graphene's π-conjugated network and its surface functional groups [13–17]. Despite this progress, several challenges remain unresolved. A major limitation is the difficulty in distinguishing DA from structurally related interferents such as ascorbic acid (AA), uric acid (UA), and other neurotransmitters (e.g. serotonin and norepinephrine), which exhibit overlapping redox potentials. Achieving a high sensitivity at nanomolar concentrations, essential for early diagnosis, also remains difficult. Although the use of graphene-based nanocomposites with transition- or noble metals and polymers can reduce the detection limit (LOD), they often suffer from drawbacks such as a poor stability, nonspecific adsorption, complex surface chemistry, poor reproducibility, limited selectivity, and environmental concerns [18, 19]. In contrast, pure, unmodified graphene-based materials have been less extensively studied and seldom achieve a simultaneous combination of desirable electrochemical features, including broad linear detection ranges (LR), a low LOD, a high sensitivity, a long-term stability and an excellent selectivity. Many existing unmodified graphene-based sensors exhibit either narrow detection ranges or an insufficient selectivity in real samples, limiting their applicability in clinical diagnostics [17, 18, 20]. These shortcomings often arise from difficulties in precisely controlling the structural and surface characteristics of graphene-based materials during synthesis and functionalisation. To address this gap, it is essential to investigate how the size of graphite precursors influences GO synthesis, its subsequent reduction to rGO, and the resulting structural and electrochemical properties. Variations in graphite flake size determine the oxidation degree, defect formation, and surface functionalities, which in turn affect the electrochemical behaviour. Unlike previous studies that mainly focused on composite-based strategies, this work systematically explores the impact of precursor particle size on dopamine sensing performance.

In this study, we examine GO derived from graphite flakes of different sizes (≤50 and ≥149–≤840 μm), its thermal reduction to rGO, and the structural and chemical properties of the resulting materials, and demonstrate their application in fabricating a highly sensitive electrochemical DA sensor. Our findings undoubtedly offer insights into the relationships between the precursor size, reduction process, material properties and sensor efficiency, contributing to the advancement of graphene-based sensor technologies.

EXPERIMENTAL

Materials and reagents

Graphite powders used for the synthesis was of extra pure grade. According to the manufacturer's data (Merck), their particle size was ≤50 μm (≥99.5%) and ≥149 – ≤840 μm (99.9%). All other chemical reagents were purchased from Sigma-Aldrich (USA) and were of analytical grade unless otherwise specified.

Preparation of GO using traditional Hummers' method

For the synthesis of GO, graphite powders with particle sizes ≤50 μm (Gr_1) and ≥149–≤840 μm (Gr_2) were used. Graphite (6 g) was oxidised following the Hummers' method [21]. Briefly, graphite was dispersed in a cold mixture (3°C) of

concentrated H_2SO_4 (240 mL) and $NaNO_3$ (3 g), after which $KMnO_4$ (30 g) was gradually added under stirring, keeping the temperature below 20°C. The mixture was maintained at room temperature for 3 days, then stirred at 35°C for 1 h and diluted with 276 mL of water. It was subsequently heated to 70°C for 15 min, followed by the addition of 840 mL of water and 20 mL of 30% H_2O_2. The resulting suspension was filtered and washed with 0.5 L of 10 wt% HCl solution to remove metal ions, and further purified by dialysis (MWCO 10.000–20.000 Da) against distilled water until sulfate-free (pH ≈ 5.0). Finally, the suspension was filtered, and the obtained brown solid was dried in a vacuum desiccator to constant weight. The products were labelled as GO_1 and GO_2, where GO_1 corresponds to graphene oxide synthesised from graphite with particle sizes ≤50 μm, and GO_2 refers to graphene oxide obtained from graphite with particle sizes ranging from 149 to 840 μm. The synthesis steps are schematically illustrated in Fig. 1.

Preparation of rGO

Thermal reduction of GO was carried out using the thermal shock method. In this procedure, GO powder was placed in a quartz tube and rapidly introduced into a preheated furnace. Each GO sample (0.1 g) was reduced in a horizontal tubular furnace at 800°C for 30 min under an Ar atmosphere with a flow rate of 60 mL min^{-1}. Two rGO samples were thus obtained and labelled according to the particle size of the graphite precursor – rGO_1 and rGO_2. A schematic illustration of the thermal reduction procedure is presented in Fig. 2.

Material characterisation

Scanning electron microscopy (SEM) analysis was carried out using a Hitachi SU-70 microscope (Tokyo, Japan) operated at an accelerating voltage of 10.0 kV and a magnification of 50,000×. Before imaging, the specimens were coated with a ~4.4 nm silver layer using a Q150T ES turbo-pumped sputter coater (Quorum Technologies,

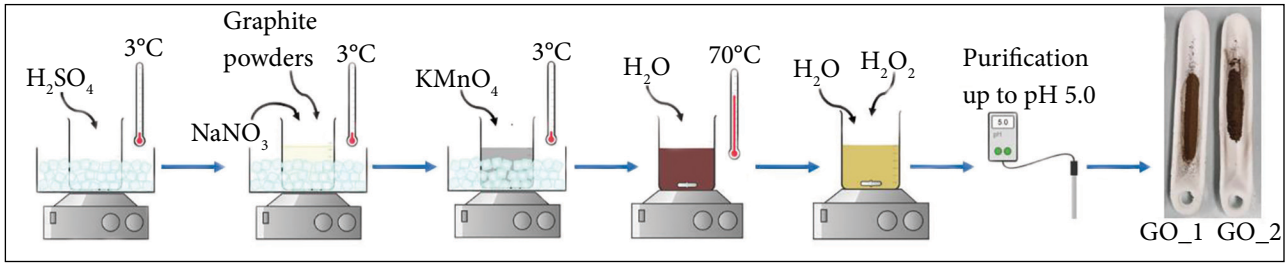

Fig. 1. Schematic illustration of the synthesis of graphene oxide from graphite powders of different particle sizes using the Hummers' method

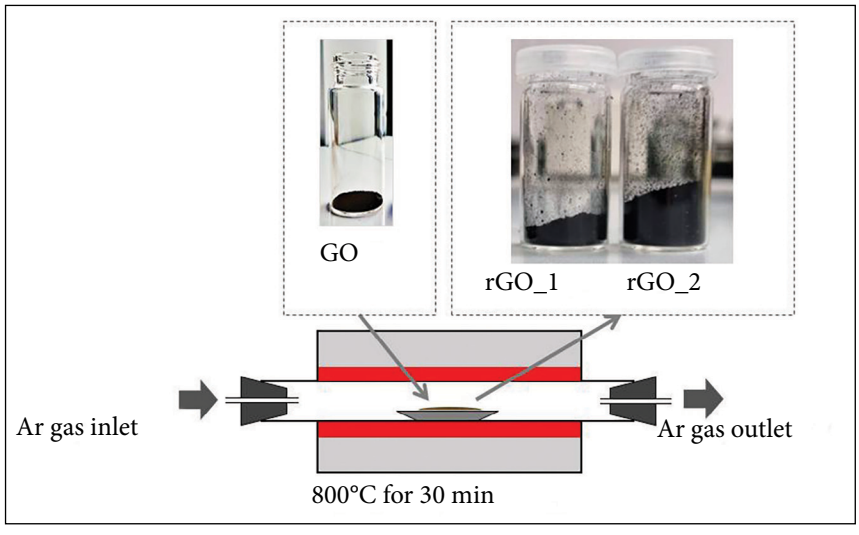

Fig. 2. Schematic representation of the thermal reduction of GO to rGO

Lewes, UK) to ensure sample conductivity and prevent charge accumulation during the SEM analysis.

Raman measurements were performed with an inVia spectrometer (Renishaw, UK) equipped with a microscope and a CCD detector cooled to –70°C. Excitation was provided by a 532 nm laser, focused through a 20 × /0.40 NA objective, and the spectra were dispersed with an 1800 grooves mm^{-1} grating. Each spectrum was collected with an acquisition time of 100 s, while the laser power was restricted to 0.4 mW to minimise sample damage. Data processing was carried out using the GRAMS/A1 8.0 software (Thermo Scientific), and the spectral bands were analysed by the Gaussian–Lorentzian fitting function.

X-ray photoelectron spectroscopy (XPS) analysis was carried out on a Kratos Axis Supra spectrometer (Kratos Analytical, Kyoto, Japan) using monochromatic Al Kα radiation (1486.69 eV). The spectra were calibrated to the C 1s peak at 284.6 eV and acquired with a pass energy of 20 eV. Data were processed in CASA XPS with Shirley background subtraction and fitted using Gaussian–Lorentzian functions.

X-ray diffraction (XRD) patterns were recorded on a Rigaku Miniflex II diffractometer (Neu-Isenburg, Germany) using Cu Kα (λ = 1.5418 Å) radiation at 30 kV and 15 mA. Interlayer spacing (d) was calculated from Bragg's law, while the crystallite size (L) was estimated using the Debye–Scherrer equation [22].

Nitrogen adsorption–desorption isotherms were obtained at 77 K using a TriStar II 3020 analyzer (Micromeritics, Norcross, GA, USA). Prior to measurements, samples were degassed under N_2 at 120°C for 2 h. The specific surface area (S_{BET}) was calculated using the Brunauer–Emmett–Teller (BET) method, and the pore size distribution was evaluated by the Barrett–Joyner–Halenda (BJH) approach.

The electrochemical response of dopamine at rGO-modified electrodes (GCE/rGO) was investigated using differential pulse voltammetry (DPV) in a conventional three-electrode cell, consisting of a platinum wire counter electrode, an Ag/AgCl reference electrode, and a bare or rGO-modified glassy carbon (GC) electrode (3.0 mm diameter) as the working electrode. For electrode modification, a PalmSens BV GC electrode (Houten, The Netherlands) was polished with alumina slurry (0.05 μm, Kemet, UK), ultrasonically cleaned in water and subsequently coated with the rGO sample. Specifically, 1.0 mg of rGO was dispersed in 1.0 mL of 0.05% Nafion solution and sonicated for 30 min, after which 10 μL of the suspension was drop-cast onto the electrode surface and dried at room temperature. The modified electrodes were labelled GCE/rGO_1 and GCE/rGO_2.

Electrochemical experiments were carried out at room temperature using a PalmSens4 potentiostat/galvanostat (PalmSens BV, Houten, The Netherlands). DPV measurements were performed in 0.1 M phosphate buffer (PB) solution (pH 7.2) under the following parameters: potential window –1.0 to +1.0 V, potential step 5 mV, scan rate 50 mV s^{-1}, pulse width 50 ms and pulse amplitude 50 mV. The limit of detection (LOD) was determined as the minimum DA concentration providing a signal above the background, according to the equation [23]:

$$\mathrm{LOD} = 3\sigma/s, \tag{1}$$

where σ is the standard deviation of the response, and s is the slope of the linear calibration curve. The sensitivity of the electrode was defined as the slope normalised to the geometric surface area of the GC electrode [24]:

$$\mathrm{Sensitivity} = s/A, \tag{2}$$

where A is the geometric area of the GC electrode, and s is the slope of the linear part of the calibration curve.

RESULTS

Figure 3 shows the XPS wide-scan spectra and the relative surface elemental composition of GO_1, GO_2, rGO_1 and rGO_2 samples. The survey spectra (Fig. 3a) reveal the presence of characteristic peaks corresponding to C 1s, O 1s, and trace amounts of S 2p in all samples. Sulfur detected in the GO structure likely attributed to residual sulfates introduced during the chemical oxidation of graphite. Thermal treatment of GO facilitates the removal of these sulfate groups. Notably, the oxygen-to-carbon (O/C) atomic ratio decreases significantly upon reduction of GO to

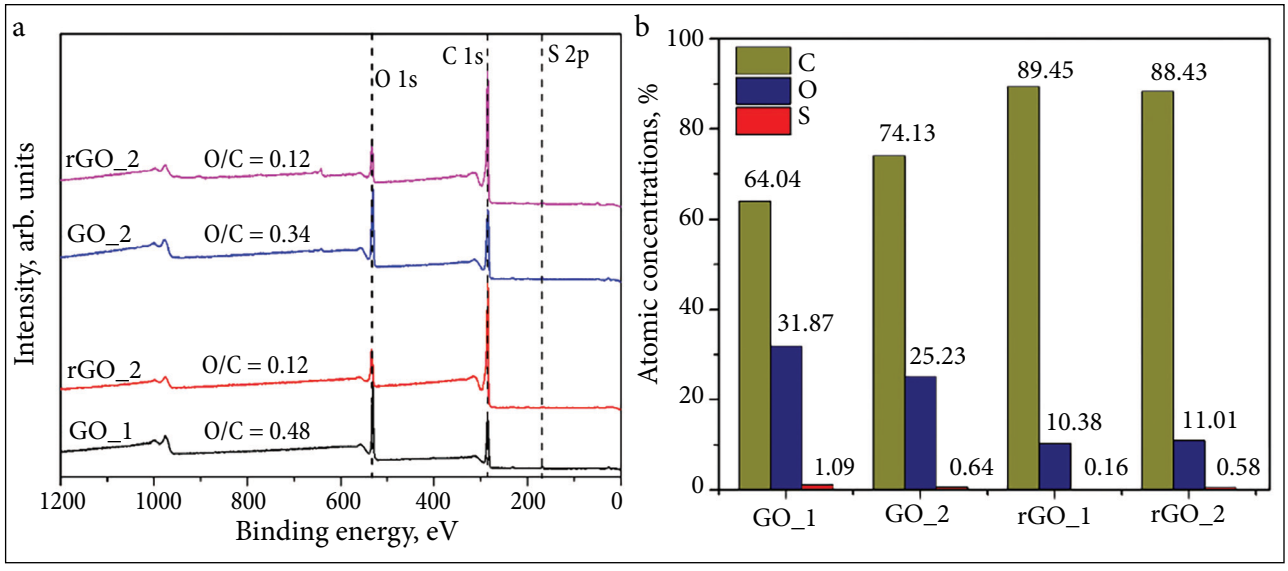

Fig. 3. Wide-scan XPS spectrum of the samples (a) and the surface composition in atomic percent (at.%) measured by XPS (b)

rGO, indicating an effective removal of oxygen-containing functional groups through the reduction process. Specifically, the O/C ratio drops from 0.48 (GO_1) and 0.34 (GO_2) to 0.12 for both rGO_1 and rGO_2. Nevertheless, residual oxygen-containing functional groups are still present in the structure. Thermal annealing reduces the oxygen content from 31.87 at.% in GO_1 and 25.23 at.% in GO_2 to 10.38 and 11.01 at.% in rGO_1 and rGO_2, respectively, resulting in partially reduced graphene oxide surfaces. These oxygen-containing functionalities ensure the suitable wettability of rGO, thereby facilitating electrolyte penetration during electrochemical testing [25]. Furthermore, the negatively charged oxygen moieties on the rGO surface may interact electrostatically with cationic DA molecules, which could contribute to enhanced sensing performance.

The high-resolution C1s spectra for both GO and rGO samples are presented in Fig. 4. For GO_1 and GO_2, the spectra were deconvoluted into five distinct components located at 284.4, 286.2, 287.3, 288.5 and 290.1 eV. The signal at 284.4 eV arises from the overlapping contributions of sp^2- and sp^3-hybridised carbon atoms, as these peaks cannot be clearly separated in XPS analysis [26]. The remaining components correspond to C–O groups (hydroxyl/epoxy, 286.2 eV), C=O groups (carbonyl, 287.3 eV), O–C=O groups (carboxyl, 288.5 eV), and π–π* shake-up transitions (290.1 eV) [27]. The same components are also observed in the rGO samples, although their relative intensities change substantially. After thermal reduction, the signals associated with oxygen functionalities decrease significantly, and the contribution from sp^2/sp^3 carbon becomes dominant (see Table 1). In addition, the peak at 290.9 eV, which is attributed to π–π* shake-up transitions resulting from the partial restoration of the conjugated π-network, is more intense in rGO than in GO, confirming the recovery of graphitic domains during the reduction process.

Raman spectroscopy was used to investigate the structural characteristics of graphite, GO and rGO. This technique provides insight into the level of disorder and defect density through analysis of the D and G bands. The obtained spectra, presented in Fig. 5, clearly illustrate the differences between pristine graphite and GO or rGO.

In graphene-related materials, the Raman spectrum is mainly characterised by the G band, arising from the in-plane stretching vibrations of sp^2-hybridised carbon atoms in both aromatic rings and chains (E_{2g} mode), and the D band, which originates from the breathing vibration of six-membered sp^2 carbon rings (A_{1g} mode) [28, 29]. In defect-free graphene, the D band is symmetry-forbidden; however, it becomes active in the presence of lattice imperfections. Another defect-related feature, the D′ band, often appears on the higher-frequency side of the G band (Fig. 5a, b). In addition, a broad band in the 1100–1200 cm^{-1} region, referred to as D*, is typically observed in GO and attributed to sp^3-hybridized carbon species [30, 31]. Moreover,

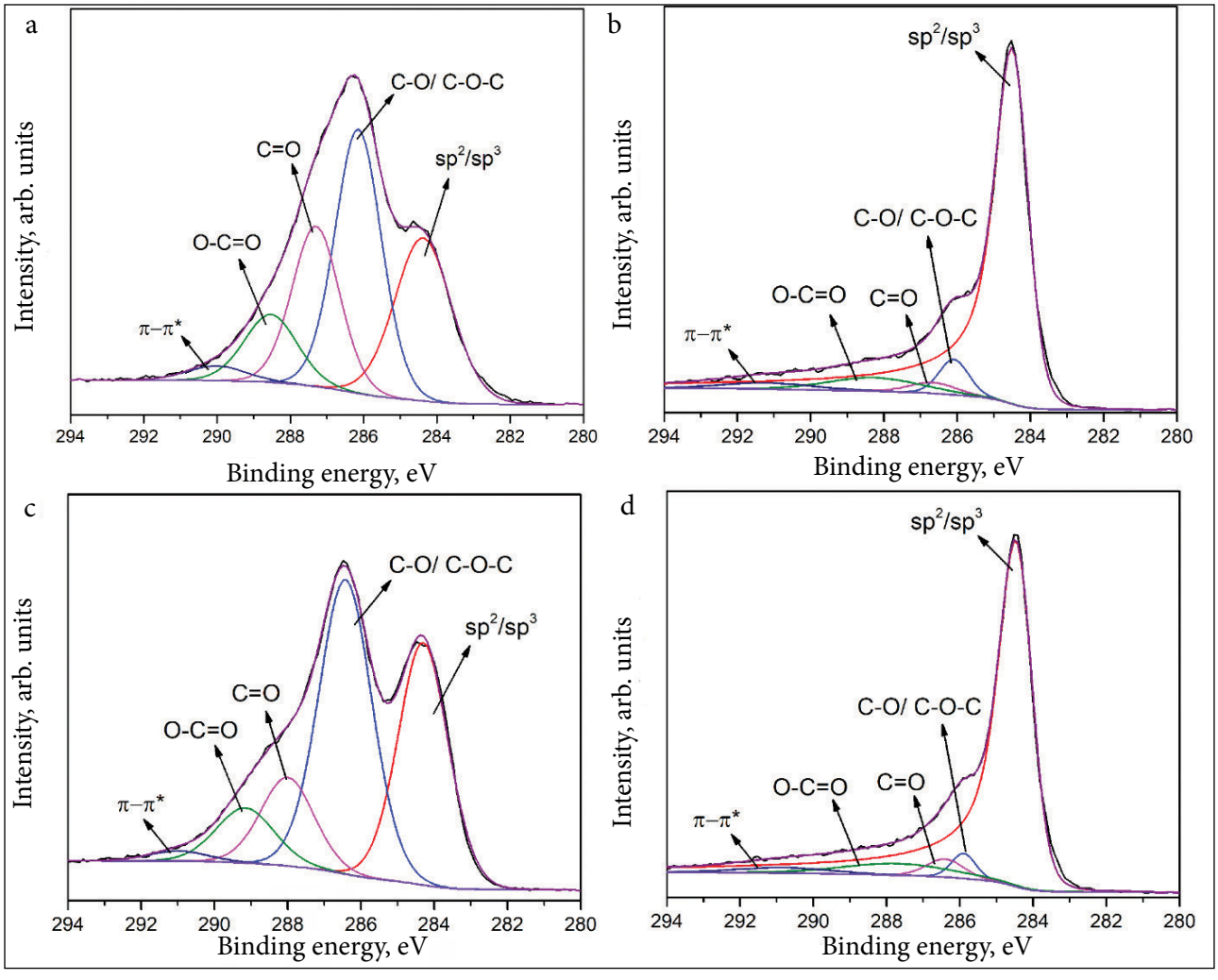

Fig. 4. C1s XPS spectra of GO and rGO samples: GO_1 (a), rGO_1 (b), GO_2 (c) and rGO_2 (c)

Table 1. **Surface distribution and relative concentration (%) of carbon and oxygen-containing functional groups in GO and rGO samples derived from C1s XPS deconvolution**

Sample	Distribution and concentration (%) of O-containing functional groups				
	C sp^2/sp^3	C-O, C-O-C	C=O	O-C=O	π-π*
GO_1	27.60	36.52	22.65	10.66	2.57
GO_2	33.49	43.08	12.97	8.80	1.66
rGO_1	83.73	5.02	2.44	6.01	2.80
rGO_2	84.83	2.97	3.31	6.36	2.53

disordered GO typically exhibits a broad D″ band in the 1500–1550 cm^{-1} region, which has been associated with the amorphous carbon phase [32].

In Figs 5a and b, which present the Raman spectra of the graphite samples, the D band is located at approximately 1351 cm^{-1}, while the G band appears near 1581 cm^{-1}. A weak D′ band is visible on the higher-frequency side of the G band at around 1620 cm^{-1}. No D* or D″ bands are observed in the graphite spectra, whereas in the GO (Fig. 5c, d) and rGO (Fig. 5e, f) samples, these bands are clearly detected at ~1200 and ~1526 cm^{-1}, respectively.

The full width at half maximum of the G band, FWHM(G), provides a valuable insight into the structural characteristics of carbon materials [30, 32, 33]. Accordingly, the Raman spectra in the 1000–1800 cm^{-1} region were deconvoluted into four Lorentzian–Gaussian components. The experimentally

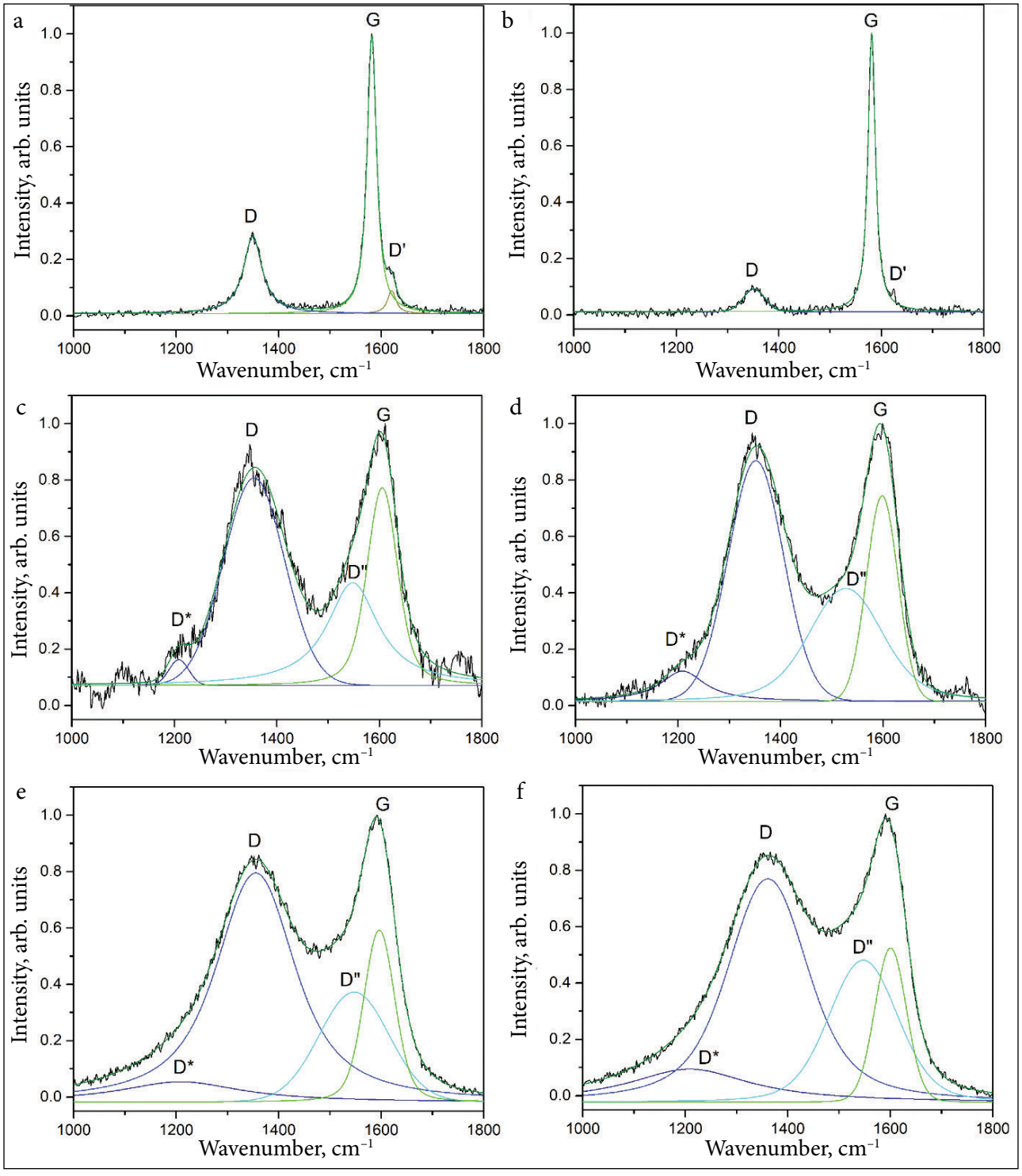

Fig. 5. Raman spectra of graphite, GO and rGO samples with fitted Lorentzian–Gaussian (D and G bands): graphite with 50 µm particle size (a), graphite with ≥149–≤840 µm particle size (b), GO_1 (c), GO_2 (d), rGO_1 (e) and rGO_2 (f)

determined FWHM(G) values can then be applied to estimate the crystallite size (L_a) [34, 35]:

$$L_a = \frac{l_c}{2} \ln\left[\frac{c}{\text{FWHM(G)-FWHM(G}_0\text{)}}\right], \qquad (3)$$

where the photon coherence length l_c = 32 nm, C = 95 cm^{-1}, and FWHM(G) and FWHM(G_0) represent the widths of the G band for the investigated sample and for undoped pristine graphene (15 cm^{-1}), respectively. The equation is valid for measuring L_a between 32 and 2.8 nm [35]. The corresponding G

Table 2. **Raman parameters determined for graphite, GO and rGO samples**

Sample	FWHM, cm^{-1}	L_a, nm	I_D''/I_G
Graphite (50 μm particle size)	22.04	41.6	–
Graphite (≥149–≤840 μm particle size)	17.43	58.7	–
GO_1	70.65	8.6	0.44
GO_2	72.31	8.1	0.42
rGO_1	71.58	8.3	0.37
rGO_2	72.69	8.0	0.48

band parameters and calculated L_a values are summarised in Table 2.

As shown in Table 2, the oxidation of pristine graphite leads to a pronounced increase in FWHM(G). In the case of graphite with a 50 μm particle size, FWHM(G) rises from 22.04 to 70.65 cm^{-1} (for GO_1). Similarly, in the case of graphite with ≥149–≤840 μm particle size, FWHM(G) increases from 17.43 to 72.31 cm^{-1} (for GO_2). This broadening of the G band indicates an increased density of sp^3-related defects and a smaller crystallite size [36]. These changes result from the incorporation of various oxygen functionalities, including hydroxyl, epoxy, carboxyl and carbonyl groups.

Following the thermal reduction of GO samples, the FWHM(G) values show a slight further increase, rising from 70.65 cm^{-1} for GO_1 and 72.31 cm^{-1} for GO_2 to 71.58 and 72.69 cm^{-1} for rGO_1 and rGO_2, respectively. The broadening of the FWHM(G) peak is likely associated with the elimination of oxygen-containing functional groups combined with the generation of structural defects, such as vacancies, dislocations, and surface irregularities, during the thermal reduction process [37]. In addition, the slightly greater FWHM(G) value observed for rGO_2 suggests that this sample contains a higher density of defects and imperfections compared to rGO_1. This difference can be attributed to the influence of graphite flake size on the oxidation and reduction process. Specifically, larger graphite flakes tend to entrap more intercalant species during oxidation, which, upon thermal reduction, generate a higher internal pressure that facilitates exfoliation but simultaneously induces cracking and the formation of additional defects [38, 39].

Depending on the sample, the calculated L_a values range from 8.0 to 58.7 nm (Table 2). The largest in-plane crystallite size is observed for graphite with a ≥149–≤840 μm particle size (58.7 nm), while graphite with a 50 μm particle size also exhibits relatively high values (41.6 nm). A larger L_a reflects the presence of extended graphitic domains with fewer structural imperfections. In contrast, the reduced L_a values in GO and rGO samples reflect a decrease in an aromatic cluster size, which is associated with an increased density of defects in the graphene layers arising from oxygen-containing functional groups and structural distortions introduced during thermal treatment.

The $I_{D''}/I_G$ intensity ratio is commonly used as a parameter to assess the amorphisation in graphene-related materials (Table 2). Among the samples, rGO_2 exhibits the highest fraction of amorphous carbon, with a ratio of 0.48.

XRD analysis was carried out to evaluate the structural changes occurring during the oxidation of graphite samples to GO and their subsequent reduction to rGO. The diffraction patterns of graphite, GO and rGO samples are presented in Fig. 6, while the corresponding peak positions, interlayer spacing (d_{002} and d_{001}) and crystallite sizes (D) are summarised in Table 3. The XRD pattern of graphite powders exhibits a characteristic peak at $2\theta \approx 26.4°$, corresponding to the (002) plane. The calculated interlayer spacings (d_{002}) are 0.338 nm for graphite with 50 μm particles and 0.337 nm for graphite with ≥149–≤840 μm particles. The calculated crystallite sizes (D) are 26.55 and 33.17 nm, respectively, indicating that larger graphite flakes possess more extended crystalline domains. In addition to the (002) reflection, weaker peaks assigned to the (100) plane at $2\theta = 42.36°$ and the (004) plane at $2\theta = 54.56°$ are also detected, further verifying the graphitic structure [36].

XRD analysis of the GO samples shows a distinct shift of the main diffraction peak to lower angles ($2\theta = 10.87°$ for GO_1 and $2\theta = 11.03°$ for GO_2), corresponding to the (001) reflection [40]. The calculated interlayer spacing (d_{001}) is 0.813 nm

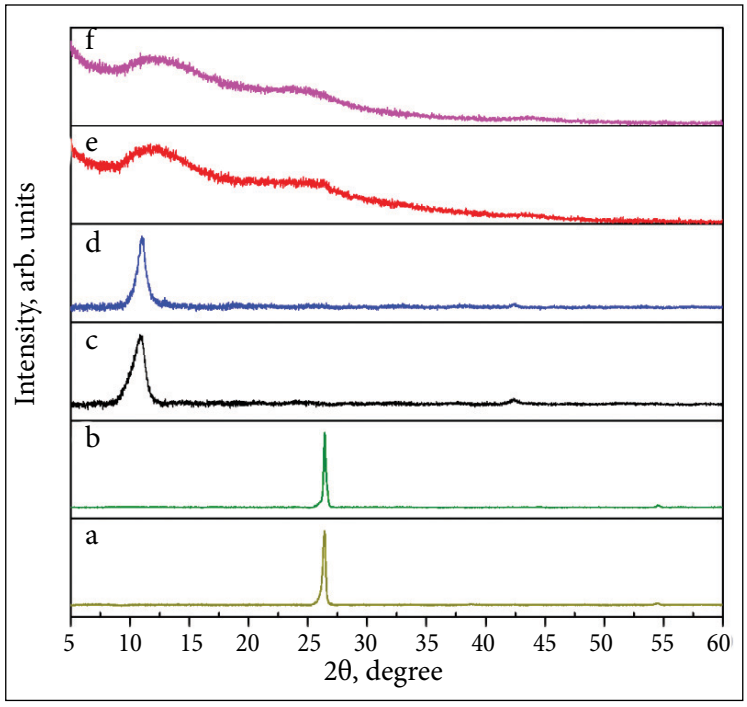

Fig. 6. XRD pattern of graphite, GO and rGO sample: graphite with 50 µm particle size (a), graphite with ≥149–≤840 µm particle size (b), GO_1 (c), GO_2 (d), rGO_1 (e) and rGO_2 (f)

for GO_1 and 0.802 nm for GO_2, indicating a successful oxidation of graphite and the incorporation of oxygen-containing functional groups. The crystallite sizes (D) are determined to be 5.82 and 9.34 nm, respectively.

The crystallite sizes obtained from Raman spectra (Table 2) were consistently larger than those calculated from XRD data (Table 3). This discrepancy can be explained by the different measurement principles of the two techniques. XRD estimates a crystallite size from the diffraction of X-rays by periodically arranged atomic planes in the crystal lattice, whereas Raman spectroscopy measures scattering of laser light perturbed by the interaction with the matter [41]. Similar findings were reported by J. Guerrero-Contreras, who demonstrated that Raman-derived crystallite sizes were higher compared with XRD data [42].

Thermal reduction of GO leads to pronounced broadening of the XRD peaks in the resulting rGO samples, indicating a decrease in crystallite size. In all cases, the main diffraction peak appears at $2\theta \approx 12.5°$, corresponding to a decrease in interlayer spacing from ~0.813 nm in GO_1 and 0.802 nm in GO_2 to ~0.707 nm in the rGO samples, resulting from the partial removal of oxygen-containing functional groups. Furthermore, this broad reflection is asymmetric, which can be attributed to the coexistence of graphitic and disordered domains within the structure. Additionally, a weaker and broader peak is observed at $2\theta \approx 26.0°$, which is most likely associated with graphite.

The morphology of the synthesised samples was investigated by scanning electron microscopy. The representative SEM images are displayed in Fig. 7.

Table 3. **XRD parameters determined for graphite, GO and rGO samples**

Sample	2θ, degree	d_{001}, nm	d_{002}, nm	D, nm
Graphite (50 µm particle size)	26.38	–	0.338	26.55
Graphite (≥149–≤840 µm particle size)	26.43	–	0.337	33.17
GO_1	10.87	0.813	–	5.82
GO_2	11.03	0.802	–	9.34

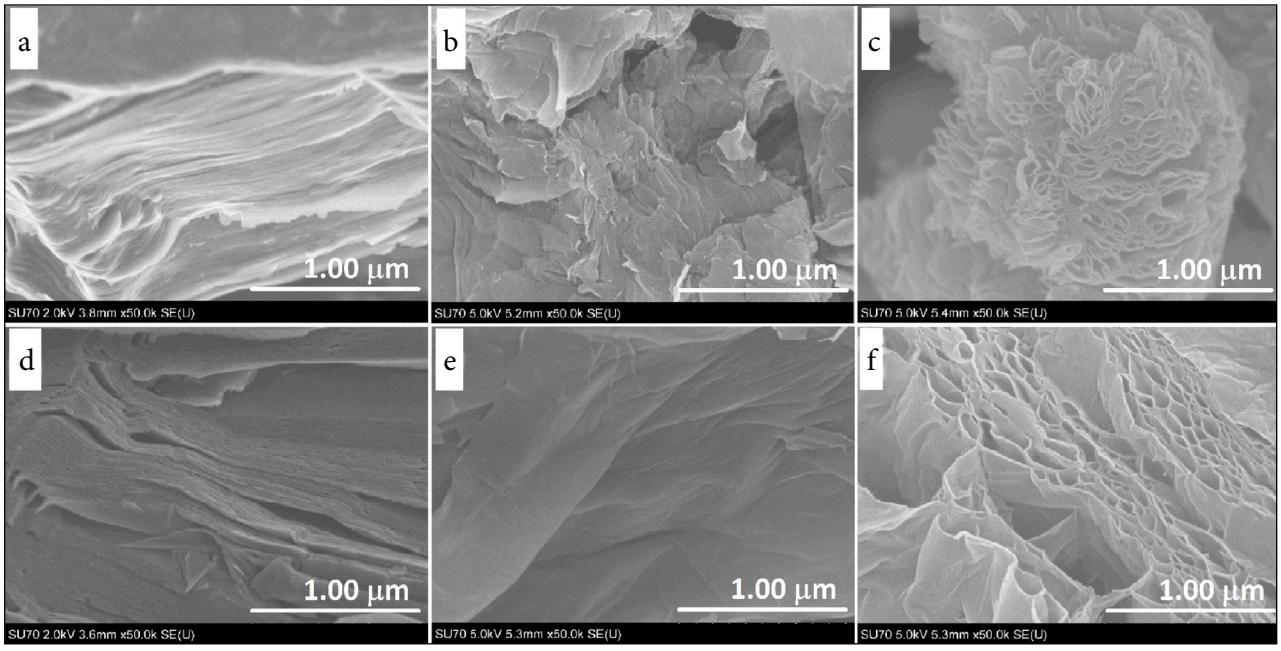

Fig. 7. SEM images of graphite with 50 μm particle size (a), GO_1 (b), rGO_1 (c), graphite with ≥149–≤840 μm particle size (d), GO_2 (e) and rGO_2 (f)

As can be seen in Figs 7a and d, both graphite samples exhibit the characteristic layered crystalline structure, which differs significantly from the morphologies observed in the other samples. Following oxidation, the graphite structure undergoes a significant transformation. This is characterised by an increase in interlayer spacing and a reduction in the number of stacked layers, leading to the corrugated and wavy morphology that is characteristic of GO. On the other hand, thermally reduced graphene oxide is composed of stacked graphene sheets and exhibits the well-known worm-like turbostratic morphology with a low bulk density. Thermal reduction produces crumpled graphene nanosheets that are randomly arranged and overlapped, resulting in slit-shaped porous structures.

The nitrogen adsorption–desorption measurements reveal differences in the textural properties of the studied samples. The corresponding data are summarised in Table 4.

Pristine graphite with a 50 μm particle size exhibits a very low BET surface area (13 $m^2\ g^{-1}$) and a total pore volume of 0.032 $cm^3\ g^{-1}$, while no reliable data could be obtained for graphite with a ≥149–≤840 μm particle size due to its nonporous nature. After oxidation, the surface area increases compared to graphite, reaching 55 $m^2\ g^{-1}$ for GO_1 and 3 $m^2\ g^{-1}$ for GO_2, indicating partial exfoliation and the incorporation of oxygen-containing groups. In contrast, thermal reduction significantly enhances the textural characteristics. rGO_1 exhibits a BET surface area of 543 $m^2\ g^{-1}$ with a total pore volume of 1.774 $cm^3\ g^{-1}$, while

Table 4. **Textural properties determined from nitrogen adsorption–desorption measurements**

Sample	S_{BET}, $m^2\ g^{-1}$	V_{tot}, $cm^3\ g^{-1}$	V_{μ}, $cm^3\ g^{-1}$	Average pore width, nm
Graphite (50 μm particle size)	13	0.032	<0.01	9.2
Graphite (≥149–≤840 μm particle size)	n.d.	n.d.	n.d.	n.d.
GO_1	55	0.045	<0.01	5.2
GO_2	3	0.003	<0.01	25.1
rGO_1	543	1.774	<0.06	9.5
rGO_2	429	1.320	<0.05	10.3

rGO_2 maintains a similarly high surface area of 429 $m^2\ g^{-1}$ and a pore volume of 1.320 $cm^3\ g^{-1}$. The pronounced increase in S_{BET} can be attributed to exfoliation caused by the thermal decomposition of oxygen-containing functional groups in GO, which is supported by the decrease in oxygen content from 31.87 at.% in GO_1 and 25.23 at.% in GO_2 to 10.38 and 11.01 at.% in rGO_1 and rGO_2, respectively (Fig. 3b). In addition, all samples exhibit predominantly meso- and macroporous structures, as evidenced by their low micropore volumes ($V_\mu < 0.06\ cm^3\ g^{-1}$) and average pore widths in a range of 5.2–25.1 nm.

Figure 8 shows the N_2 adsorption–desorption isotherms (a, b) and pore size distribution curves (c) for graphite with a 50 μm particle size, GO and rGO samples. In contrast, no isotherms are obtained for graphite with ≥149–≤840 μm particles, since this material is essentially nonporous and its surface area is too low to be detected by the BET method. This difference highlights the effect of particle size: smaller flakes provide a greater surface area and more edge sites for nitrogen adsorption, while larger flakes maintain a tightly ordered layered structure with a minimal accessible surface. Consequently, nitrogen cannot penetrate between the stacked layers, limiting adsorption to the outer surface and making isotherm analysis impossible.

According to the IUPAC classification [43], the recorded isotherms correspond to type IV(a) with H3 hysteresis loops. Such isotherm profiles are characteristic of mesoporous structures, while the H3 hysteresis loops observed are often linked to plate-like particles forming slit-shaped pores, such as those found in graphene-related materials where pores are created between parallel layers. The pore

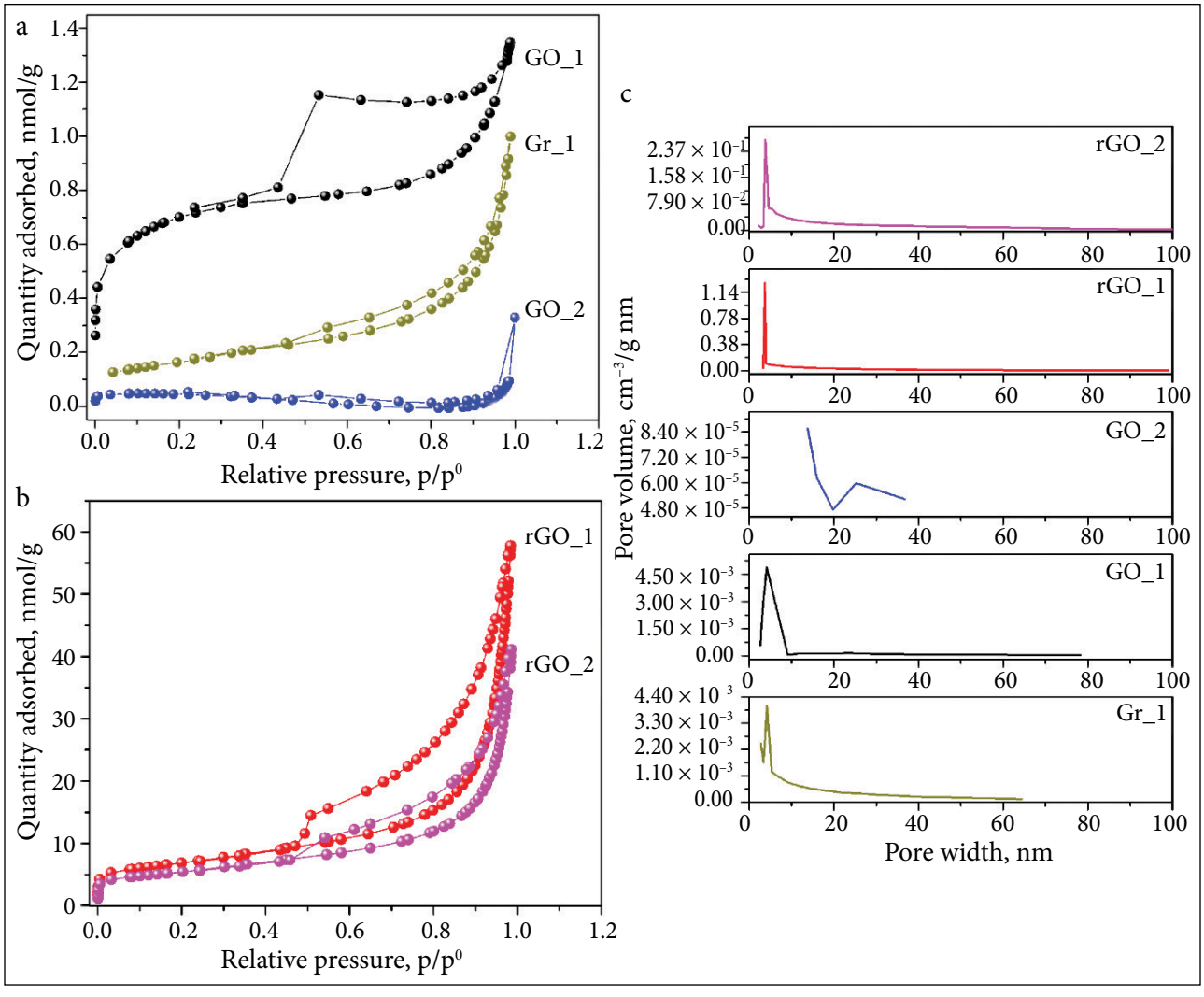

Fig. 8. N_2 adsorption–desorption isotherms (a, b) and pore size distribution plots (c) for the prepared samples

size distribution curves derived from the BJH model (Fig. 8c) further confirm the mesoporous nature of the materials, showing dominant pore widths in the 2.5–5 nm range for all samples except GO_2. In the case of GO_2, the distribution is shifted toward larger pores, with the majority of pore widths falling in the 13–27 nm range, indicating the prevalence of larger mesopores.

The rGO samples were tested for electrochemical DA detection. Figure 9a illustrates their DPV response in a PB solution (pH 7.2) containing 20 μM DA.

As seen in Fig. 9a, both constructed rGO_1/GCE and rGO_2/GCE sensors exhibited significantly higher DA peak currents at approximately +0.20 V compared to the bare GCE. The enhanced current response of the rGO-modified electrodes indicates an improved electrochemical activity, which can be ascribed to a larger surface area, and abundance of defect sites introduced by the thermal reduction of GO. Moreover, the rGO_2/GCE sensor exhibited the most pronounced anodic peak current, suggesting that its structural characteristics provide a greater density of electroactive sites and more favourable conditions for DA adsorption and oxidation compared to rGO_1/GCE. These results demonstrate that the physicochemical features of the rGO materials, dictated by the size of the graphite precursor, play a critical role in determining their sensing performance.

The influence of PB solution pH on the peak current and peak potential was investigated. Figure 9b shows the DPV curves recorded at different pH values for 50 μM DA. As illustrated in Figs 9b and c, the peak current of DA depends on pH, with the maximum response observed at pH 2.8. However, under these acidic conditions, the oxidation peak potential of DA is shifted further away from 0 V, and such strongly acidic media are less suitable for practical sensing because they may promote electrode surface degradation, analyte instability, or interference from

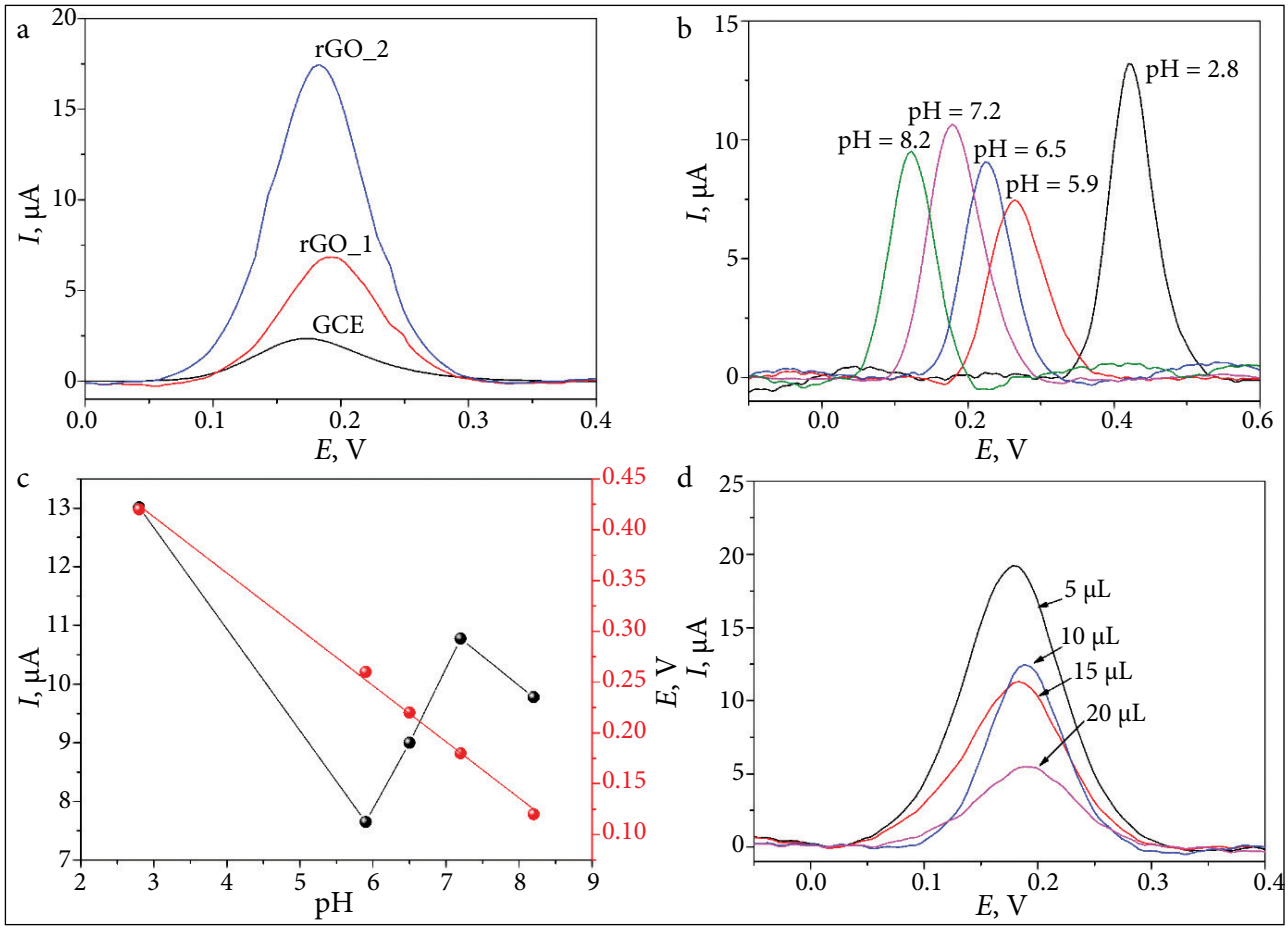

Fig. 9. DPV responses of bare GCE, rGO_1/GCE and rGO_2/GCE toward 20 μM DA in 0.1 M PB (pH 7.2) (a); at different pH values to 50 μM DA (b); the variation of anodic peak current and peak potential as a function of pH (c); the influence of rGO_1 loading volume on the DA oxidation peak current (d)

proton-coupled side reactions. When the pH was increased from 5.9 to 7.2, the peak current gradually increased, while at pH 8.2 the response decreased. Hence, pH 7.2 was selected for subsequent experiments, as it provides a strong electrochemical signal and is close to physiological conditions.

Also, the peak potential of DA electrooxidation was found to be pH-dependent. As shown in Fig. 9c, increasing the pH caused a linear negative shift in the peak potential, confirming the participation of protons in the electrode reaction. The regression equation was determined as $E(V) = -0.0553pH + 0.57845$, with an excellent correlation coefficient ($R^2 = 0.9974$). The slope obtained (–0.0553 V/pH) is close to the theoretical Nernstian value of –0.059 V/pH, suggesting that DA electrooxidation at the rGO-modified GCE proceeds via the equal number of electrons and proton, in this case, a two-electron transfer process coupled with the transfer of two protons [44].

To optimise the amount of rGO suspension on the GC electrode surface, the effect of rGO_1 loading volume on the DA oxidation signal was investigated. Figure 9d shows the dependence of the DA anodic peak current on the applied rGO_1 volume. The highest current response was observed at 5 µL of rGO_1, indicating that this amount ensures the most favourable electroactive surface area and sufficient active sites for DA oxidation. When the rGO_1 volume was further increased to 10, 15 and 20 µL, the anodic peak current decreased, which can be attributed to the partial blockage of the electrode surface and hindered electron transfer. Therefore, 5 µL of rGO_1 suspension was determined as the optimal loading for electrode modification.

The influence of scan rate on the redox behaviour of DA at rGO-modified GC electrodes was examined in 0.1 M PB solution (Fig. 10).

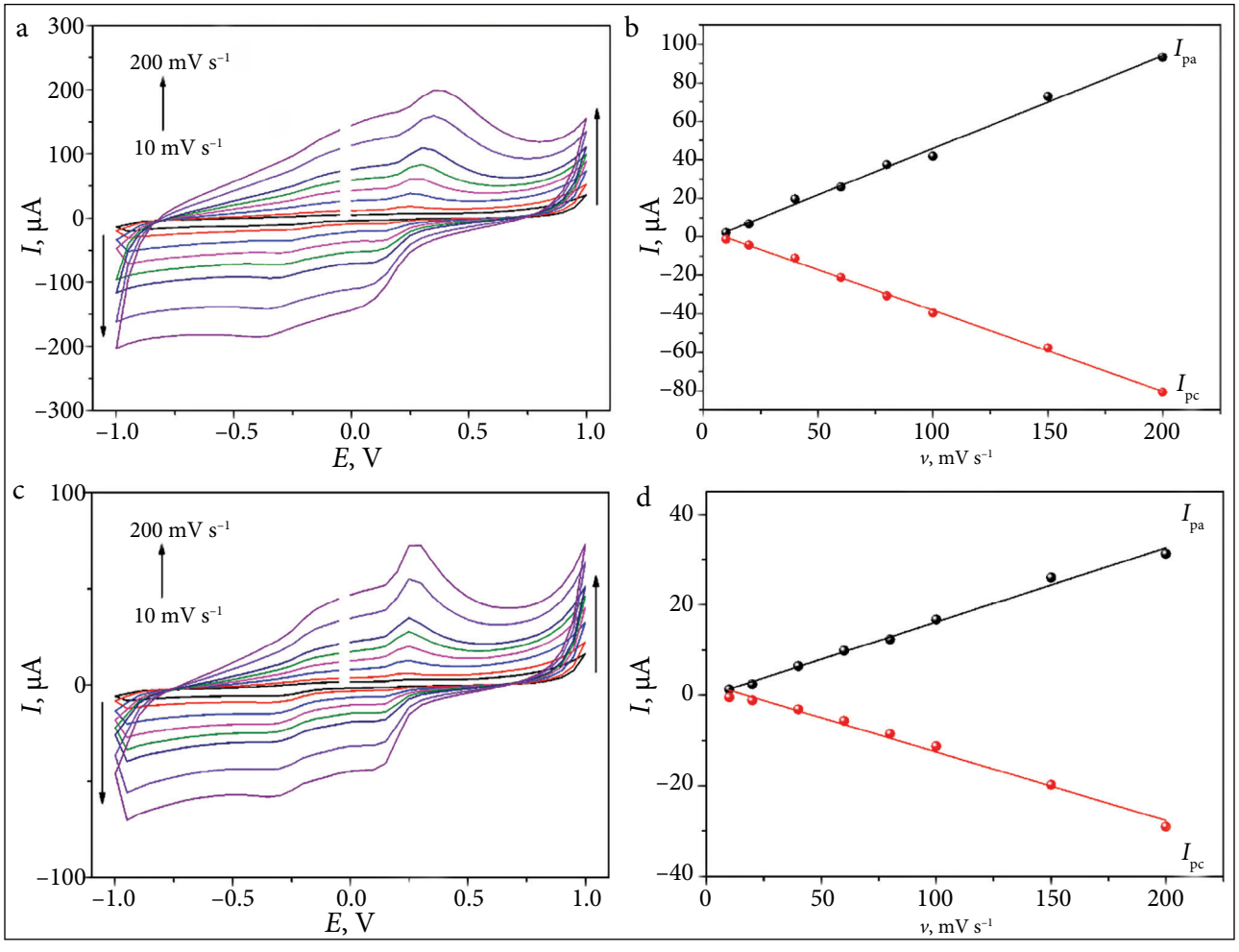

Fig. 10. CV curves of DA recorded at different scan rates from 10 to 200 mV s^{-1} for rGO_1/GCE (a) and rGO_2/GCE (c); corresponding plots of anodic and cathodic peak currents versus the scan rate for rGO_1/GCE (b) and rGO_2/GCE (d)

CV measurements were performed at scan rates between 10 and 200 mV s^{-1} to evaluate the electrode kinetics and identify the controlling factor of mass transport. As shown in Figs 10a and c, both anodic and cathodic peak currents increased progressively with the scan rate, while the corresponding peak potentials shifted slightly toward more positive (anodic) and more negative (cathodic) values. This behaviour reflects a slower electron transfer rate and a reduced reversibility of the DA redox process at higher scan rates. Furthermore, a linear relationship between both anodic and cathodic peak currents and the scan rate was observed over the investigated range (Figs 10b, d). For rGO_1/GCE, the regression equations were I_{pa} (μA) = 0.4816x – 2.277 (R^2 = 0.9949) and I_{pc} (μA) = –0.4211x + 3.9158 (R^2 = 0.9982), while for rGO_2/GCE, they were I_{pa} (μA) = 0.1641x – 0.2123 (R^2 = 0.9934) and I_{pc} (μA) = –0.1512x + 2.6282 (R^2 = 0.9881). These strong linear correlations confirm that the electrochemical redox process of DA at rGO-modified GC electrodes is predominantly adsorption-controlled [44].

DPV measurements were carried out to quantitatively evaluate the electrochemical response of DA at rGO-modified electrodes. Figures 11a and b display the DPV curves obtained for different DA concentrations using rGO_1/GCE and rGO_2/GCE, respectively.

In both cases, a distinct anodic peak appeared at approximately +0.19 V, corresponding to the oxidation of dopamine. The peak current increased proportionally with the DA concentration for both electrodes. For rGO_1/GCE (Fig. 11a), the current response increased steadily in a range of 0–59.6 μM DA, after which a decrease in anodic peak intensity was observed at higher concentrations. In contrast, the rGO_2/GCE electrode showed a linear increase

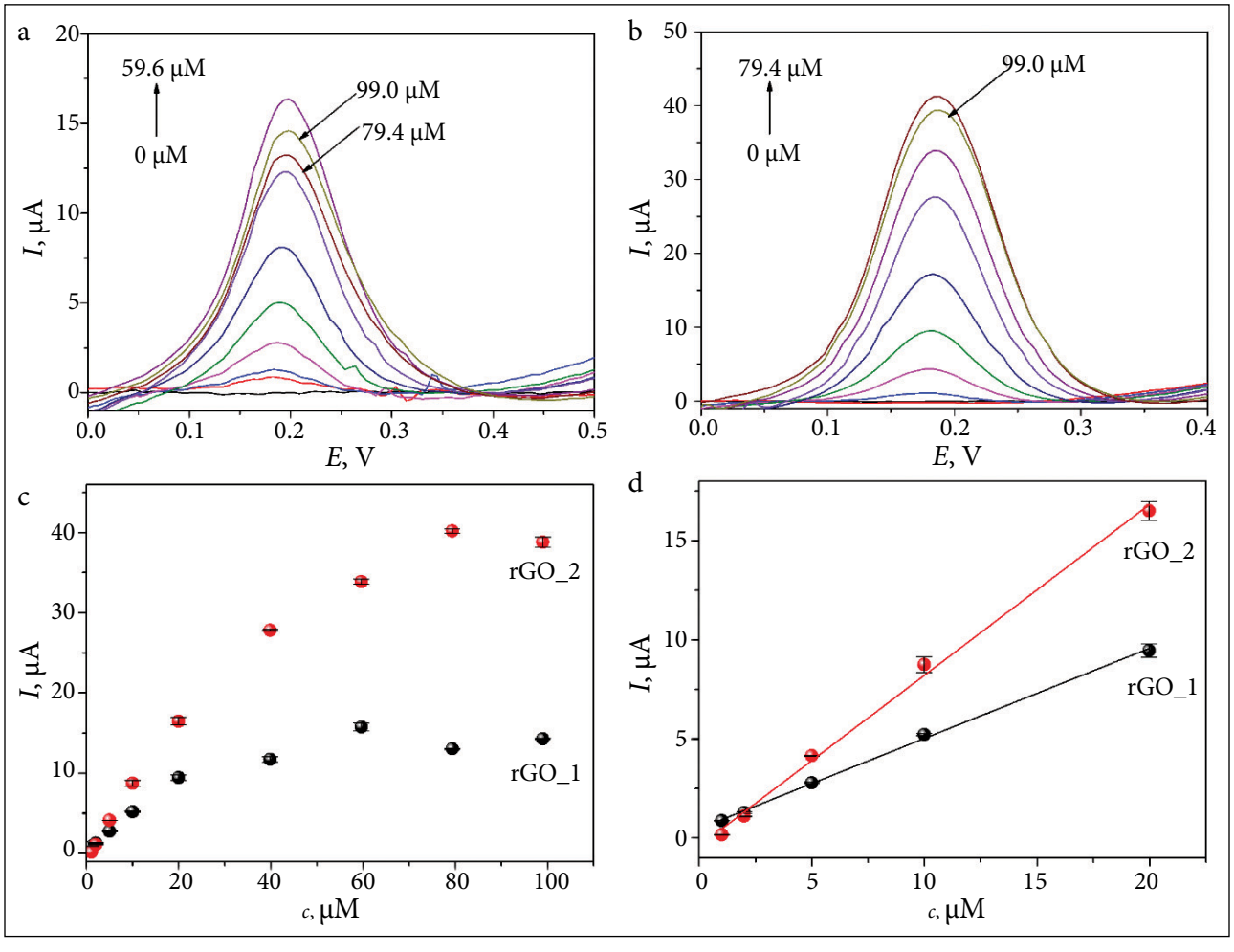

Fig. 11. DPV responses of rGO_1/GCE (a) and rGO_2/GCE (b) toward increasing DA concentrations; the calibration plots of the anodic peak current versus the DA concentration for both electrodes (c); the linear range of the calibration curves (d)

in peak current from 0 to 79.4 μM DA, with a subsequent decrease at concentrations above this level. The reduction in current at higher concentrations can be attributed to the formation of thicker surface layers due to DA or impurity adsorption, surface fouling as well as the partial blocking of pores and electroactive sites.

As shown in Figs 11c and d, the oxidation peak current of DA on both rGO_1/GCE and rGO_2/GCE electrodes exhibited a linear increase with the DA concentration in a range of 1–19.96 μM. The linear regression equation for rGO_1/GCE was $I(\mu A) = 0.4553x + 0.476$ ($R^2 = 0.9987$), while that for rGO_2/GCE was $I(\mu A) = 0.8618x + 0.4029$ ($R^2 = 0.9968$). The LOD values of DA were calculated as 61.55 nM for rGO_1/GCE and 98.17 nM for rGO_2/GCE. The corresponding sensitivities were 6.44 and 12.20 μA μM^{-1} cm^{-2} for rGO_1/GCE and rGO_2/GCE, respectively. These results indicate that although both electrodes are suitable for DA detection, rGO_2/GCE provides a higher sensitivity. The higher sensitivity can be attributed to the structural and surface characteristics. Although both rGO samples exhibit comparable oxygen-to-carbon ratios after thermal reduction (O/C ≈ 0.12), rGO_2 retains a slightly higher concentration of oxygen-containing functional groups (Fig. 3b). Such residual oxygen functionalities improve surface wettability and promote electrostatic interactions with cationic DA molecules, thereby enhancing the adsorption-controlled process. Importantly, the higher defect density and amorphous carbon fraction in rGO_2, as evidenced by its broader FWHM(G) (72.69 cm^{-1} vs 71.58 cm^{-1} for rGO_1) and higher $I_{D''}/I_G$ ratio in Raman spectra (0.48 vs 0.37 for rGO_1), generate more reactive edge sites for DA oxidation, thereby increasing the overall sensitivity of the electrode.

Compared with metal-free rGO-based sensors reported in the literature, the proposed electrodes exhibit a comparable or slightly better electrochemical performance in terms of LOD and sensitivity [14, 45–48]. Based on these promising results, future studies could be directed toward evaluating long-term stability, reproducibility and selectivity in the presence of potential interfering analytes, thereby extending the applicability of these sensors to more complex real-sample environments.

CONCLUSIONS

In this study, reduced graphene oxide (rGO) was synthesised from graphite powders of two distinct particle sizes using the Hummers' method followed by thermal shock reduction. The resulting samples, rGO_1 (derived from smaller graphite particles) and rGO_2 (from larger flakes), were thoroughly characterised to assess the influence of precursor size on structural, chemical and electrochemical properties. XPS, Raman, XRD, SEM, and nitrogen sorption analyses confirmed the successful removal of oxygen-containing functional groups after reduction, while also revealing differences in crystallite size, defect density, and porosity that strongly depended on the graphite precursor.

Electrochemical investigations demonstrated that both rGO_1/GCE and rGO_2/GCE electrodes exhibited an excellent electrocatalytic activity toward dopamine oxidation, with significantly enhanced responses compared to the bare GCE. Both electrodes achieved the linear detection of dopamine in a range of 1–19.96 μM, with detection limits of 61.55 nM (rGO_1) and 98.17 nM (rGO_2). While rGO_1 demonstrated a lower detection limit, rGO_2 exhibited a higher sensitivity, which can be attributed to its greater defect density and higher fraction of residual oxygen functionalities that improve the wettability and adsorption of dopamine molecules.

These findings highlight that the electrochemical performance of rGO-based electrodes can be tuned through a careful selection of the graphite precursor size. Such control over material properties provides a valuable route for tailoring rGO nanomaterials for electrochemical sensing applications, opening new opportunities for their use in bioanalytical detection systems.

Received 2 August 2025
Accepted 31 August 2025

References

1. W. Liu, G. Speranza, *ACS Omega*, **6**, 6195 (2021).
2. N. Borane, R. Boddula, N. Odedara, et al., *Nano-Struct. Nano-Objects*, **39**, 101282 (2024).
3. N. Morimoto, T. Kubo, Y. Nishina, *Sci. Rep.*, **6**, 21715 (2016).
4. D. Dhamodharan, P. P. Ghoderao, V. Dhinakaran, et al., *J. Ind. Eng. Chem.*, **106**, 20 (2022).

5. J. Wu, H. Lin, D. J. Moss, K. P. Loh, B. Jia, *Nat. Rev. Chem.*, **7**, 162 (2023).
6. H. Ahmad, M. Fan, D. Hui, *Compos. Part B Eng.*, **145**, 270 (2018).
7. Anjali, A. Mishra, M. Khurana, B. Pani, S. K. Awasthi, *ChemistrySelect*, **10**, e202404742 (2025).
8. R. Singh, M. S. Samuel, M. Ravikumar, S. Ethiraj, M. Kumar, *Environ. Res.*, **243**, 117830 (2024).
9. C. A. Ramirez, A. R. Thiruppathi, O. Ozoemena, A. Chen, *Can. J. Chem.*, **102**, 667 (2024).
10. H. C. Ananda Murthy, K. Gebremedhn Kelele, C. R. Ravikumar, et al., *Results Chem.*, **3**, 100131 (2021).
11. S. R. Benjamin, E. J. Miranda Ribeiro Júnior, *Curr. Opin. Environ. Sci. Health*, **29**, 100381 (2022).
12. L. Speranza, M. C. Miniaci, F. Volpicelli, *Biomedicines*, **13**, 492 (2025).
13. W. T. Wahyuni, S. A. Hasnawati Ta'alia, A. Y. Akbar, et al., *RSC Adv.*, **14**, 27999 (2024).
14. J. Gaidukevic, R. Aukstakojyte, J. Barkauskas, et al., *Appl. Surf. Sci.*, **592**, 153257 (2022).
15. A. Cernat, G. Ștefan, M. Tertis, C. Cristea, I. Simon, *Bioelectrochemistry*, **136**, 107620 (2020).
16. M. Kujawska, S. K. Bhardwaj, Y. K. Mishra, A. Kaushik, *Biosensors*, **11(11)**, 433 (2021).
17. A. Pandikumar, G. T. Soon How, T. P. See, et al., *RSC Adv.*, **4**, 63296 (2014).
18. A. Karim, M. Yasser, A. Ahmad, et al., *J. Electroanal. Chem.*, **959**, 118157 (2024).
19. R. G. State, J. F. van Staden, *Electrochem. Sci. Adv.*, **2**, e2100040 (2022).
20. C. Ferrag, K. Kerman, *Front. Sens.,* **1**, 583822 (2020).
21. W. S. Hummers Jr., R. E. Offeman, *J. Am. Chem. Soc.*, **80**, 1339 (1958).
22. S. A. Hassanzadeh-Tabrizi, *J. Alloys Compd.*, **968**, 171914 (2023).
23. C. E. Ott, *Analyst*, **149**, 4295 (2024).
24. D. A. Aikens, *J. Chem. Educ.*, **60**, A25 (1983).
25. J. Sun, C. Hu, Z. Liu, H. Liu, J. Qu, *Carbon*, **145**, 140 (2019).
26. B. Lesiak, L. Kövér, J. Tóth, et al., *Appl. Surf. Sci.*, **452**, 223 (2018).
27. D. Y. Kornilov, S. P. Gubin, *Russ. J. Inorg. Chem.*, **65**, 1965 (2020).
28. A. C. Ferrari, *Solid State Commun.*, **143**, 47 (2007).
29. R. Trusovas, G. Račiukaitis, G. Niaura, et al., *Adv. Opt. Mater.*, **4**, 37 (2016).
30. S. Claramunt, A. Varea, D. López-Díaz, et al., *J. Phys. Chem. C*, **119**, 10123 (2015).
31. G. T. T. Le, J. Manyam, P. Opaprakasit, et al., *Diamond Relat. Mater.*, **89**, 246 (2018).
32. A. C. Ferrari, J. Robertson, *Phys. Rev. B*, **64**, 075414 (2001).
33. R. Yuan, Y. Guo, I. Gurgan, et al., *Carbon*, **238**, 120214 (2025).
34. A. Jorio, A. G. Souza Filho, *Annu. Rev. Mater. Res.*, **46**, 357 (2016).
35. J. Ribeiro-Soares, M. E. Oliveros, C. Garin, et al., *Carbon*, **95**, 646 (2015).
36. G. Levi, M. Causà, L. Cortese, P. Salatino, O. Senneca, *Appl. Energy Combust. Sci.*, **1–4**, 100006 (2020).
37. M. Guo, H. Yuan, K. Ni, et al., *Adv. Sci.*, **12**, 2410088 (2025).
38. Z. Benzait, L. Trabzon, *ACS Omega*, **7**, 37885 (2022).
39. S. S. Shojaeenezhad, M. Farbod, I. Kazeminezhad, *J. Sci. Adv. Mater. Devices*, **2**, 470 (2017).
40. T. Taniguchi, L. Nurdiwijayanto, N. Sakai, et al., *Carbon*, **202**, 26 (2023).
41. P. J. Larkin, *Infrared and Raman Spectroscopy*, 2nd edn., Ch. 2, Elsevier, Amsterdam (2018).
42. J. Guerrero-Contreras, F. Caballero-Briones, *Mater. Chem. Phys.*, **153**, 209 (2015).
43. S. Brunauer, P. H. Emmett, E. Teller, *J. Am. Chem. Soc.*, **60**, 309 (1938).
44. R. T. Kachoosangi, R. G. Compton, *Anal. Bioanal. Chem.*, **387**, 2793 (2007).
45. F. Mahmood, Y. Sun, C. Wan, *RSC Adv.*, **11**, 15410 (2021).
46. L. Yang, D. Liu, J. Huang, T. You, *Sens. Actuators B*, **193**, 166 (2014).
47. K. Bala, N. Aggarwal, G. Anand, K. Ravi, N. Kumar, *ECS J. Solid State Sci. Technol.*, **14**, 021002 (2025).
48. F. Gao, X. Cai, X. Wang, et al., *Sens. Actuators B*, **186**, 380 (2013).

Dovilė Burakovaitė, Rūta Rasikė, Vilius Čižas, Gediminas Niaura, Tomas Murauskas, Rasa Pauliukaitė, Justina Gaidukevič

GRAFITO DALELIŲ DYDŽIO ĮTAKA REDUKUOTO GRAFENO OKSIDO FIZIKINĖMS IR CHEMINĖMS SAVYBĖMS BEI DOPAMINO NUSTATYMO EFEKTYVUMUI